



**HAL**  
open science

# An optimally-controlled RANS Actuator force model for efficient computations of tidal turbine arrays

Vincent Clary, Thibault Oudart, Philippe Larroudé, J. Sommeria, Thierry Maître

## ► To cite this version:

Vincent Clary, Thibault Oudart, Philippe Larroudé, J. Sommeria, Thierry Maître. An optimally-controlled RANS Actuator force model for efficient computations of tidal turbine arrays. *Ocean Engineering*, 2020, 212, pp.107677. 10.1016/j.oceaneng.2020.107677 . hal-03136320

**HAL Id: hal-03136320**

**<https://hal.science/hal-03136320>**

Submitted on 18 Jul 2022

**HAL** is a multi-disciplinary open access archive for the deposit and dissemination of scientific research documents, whether they are published or not. The documents may come from teaching and research institutions in France or abroad, or from public or private research centers.

L'archive ouverte pluridisciplinaire **HAL**, est destinée au dépôt et à la diffusion de documents scientifiques de niveau recherche, publiés ou non, émanant des établissements d'enseignement et de recherche français ou étrangers, des laboratoires publics ou privés.



Distributed under a Creative Commons Attribution - NonCommercial 4.0 International License

# An optimally-controlled RANS Actuator force model for efficient computations of tidal turbine arrays

V. Clary<sup>a</sup>, T. Oudart<sup>b</sup>, P. Larroudé<sup>a</sup>, J. Sommeria<sup>a</sup> and T. Maître<sup>a</sup>

<sup>a</sup>Univ. Grenoble Alpes, Grenoble INP (Institute of Engineering Univ. Grenoble Alpes), LEGI, 38000 Grenoble, France

<sup>b</sup>Artelia Eau & Environnement, 38130 Echirolles, France

## ARTICLE INFO

### Keywords:

Tidal turbine array  
Turbine wake  
Actuator  
Vertical axis turbine  
Darrieus turbine

## ABSTRACT

A steady-state Actuator force model using the RANS equations is developed to calculate the power production and the flow through arrays of tidal or river Darrieus turbines. It uses detailed three-dimensional force distributions depending on the position on the turbine, obtained beforehand by a set of blade-resolved URANS simulations of the turbine. New power coefficient and force coefficient laws depending on the local velocity instead of the upstream velocity are established and appear to be independent from the local turbine blockage in an array. Those laws are used to construct a model that adapt the Actuator force distributions to the local velocity of the flow reaching each turbine, in order to simulate each turbine functioning close to its maximum efficiency point. The model is validated against experimental measurements on a reduced-scale Darrieus turbine. A fence farm configuration and a two row farm configuration are investigated and compared to results of the same model adapted in two dimensions. The local blockage effect is more favorable for fences than for staggered turbine configurations, increasing the local velocity and the power production for each turbine.

## 1. Introduction

Tidal energy is currently undergoing fast progress, and the first deployment projects of several machines are planned at different places in the world. In the future, simplified models will be needed for choosing the location of several tens of turbines in an array and studying their influence on the hydrodynamic currents in the vast oceanic areas impacted. The wake interaction between turbines must be considered, with the influence of the velocity deficit and turbulence created by the upstream turbines in an array. The influence of the upstream turbulence intensity was clearly shown by Mycek et al. (2014) for horizontal axis tidal turbines. They measured experimentally that the wake of a turbine placed in a zone of high turbulence (15% turbulence intensity) recovered much faster than for low turbulence (3% turbulence intensity).

Our study focuses on vertical axis water turbines, which have the main advantage of being insensitive to the direction of the upstream flow. They are also less sensitive to the upstream turbulence level, as Boudreau and Dumas (2017) showed comparing the CFD results of various turbine models. A large eddy simulation (LES) conducted by Guillaud et al. (2016) showed in details the different vortices created in all parts of a Darrieus vertical axis turbine, including the arm-shaft connections and the blade tips. Those vortices lead to a big reduction of the turbine efficiency. This simulation model is the more accurate to describe the turbine behavior, yet it requires huge computational resources which is prohibitive for array optimization.

Different approaches have been used to reduce the computational costs. For axial turbines, analytical methods based on the Betz-Joukowski law (the Actuator Disk method) have been improved to take into account the confinement of stream

turbines, due to the presence of the bathymetry, free surface and the other adjacent turbines (Garrett and Cummins, 2007; Whelan et al., 2009). The models were extended to an array of tidal stream turbines by Vennell (2013) or Draper and Nishino (2014). Simplified CFD models seem promising. At the oceanic scale, large domains and long duration are computed thanks to 2D models, in order to simulate properly the effects of the tides at a potential site all along the year. Two different approaches exist to compute the effect of a tidal turbine: it can be modeled by a friction force on the bottom (Kramer and Piggott, 2016), or by adding a force source term in the momentum equations (Thiébot et al., 2016), both methods representing the action of the turbine on the mean flow in the vertical water column with significantly the same results. Three-dimensional simulations might be useful to take into account the 3D characteristic of the flow and the bathymetry more precisely as in Nguyen et al. (2019) or Thiébot et al. (2020). Wimshurst and Willden (2016) showed using an Actuator Disk (AD) approach that a turbine at a location where water depth is diminishing (in the current direction) produces less power than the same turbine at a location with increasing water depth. This is due to modifications in the boundary layer, as turbines are often placed at elevations that are still impacted by the velocity reduction in the bed boundary layer.

To improve AD models, the blade-element method embedded in a RANS solver (RANS-BE) can be used for the different types of turbines, to calculate the forces to impose in the so-called Actuator Line models. A force distribution depending on the position on the turbine and depending on time is used instead of the uniform force distribution of AD models. Such simulations were done for axial turbines using the RANS approach for modeling turbulence (Edmunds et al., 2017), with a good accuracy. The method to obtain the force distribution seems crucial, especially for Darrieus

 [thierry.maitre@legi.grenoble-inp.fr](mailto:thierry.maitre@legi.grenoble-inp.fr) (T. Maître)

turbines where the stall phenomenon occurs. In their Actuator Line Method, Shamsoddin and Porté-Agel (2014), Mendoza et al. (2019) and Grondeau et al. (2019) calculated the force distribution on Darrieus turbine blades with a semi-empirical dynamic stall model. They used the LES turbulence model and were able to calculate the wake of one turbine with a great accuracy.

In array configurations, the flow reaching each turbine is modified due to the local blockage defined as the fraction of the channel section occupied by the turbines. The behavior of the turbine for those different flow conditions will determine the distribution forces that have to be imposed. The turbine regulation is important and will act on the operating point used. Equipping the turbines with variable speed technology seems the most promising issue and allows the use of a maximum power point tracking (MPPT) system, in order to always take advantage of the best efficiency point of the turbine. The local velocity that is striking each turbine of an array must be used to calculate the best efficiency point for this flow configuration. For axial turbines, Nishino and Draper (2015) used the RANS  $k-\epsilon$  model to obtain the velocity in each cell of their Actuator Disk volume. The turbine forces are deduced using the drag coefficient value corresponding to the best efficiency point of the turbine. An elaborate Actuator cylinder method based on the RANS  $k-\omega$  SST model was developed by Shives et al. (2017) for cross flow turbines. The drag coefficient and power coefficient values were also depending on the upstream Reynolds number and turbulence intensity, in order to be accurate for different flow conditions. Satisfactory velocity deficits are achieved in the wake, thanks to the SST eddy-viscosity limiter that prevents a too fast velocity recovery.

A few array layout behaviors have been investigated in the literature. A power production law for turbines side by side in a channel (the fence configuration) was proposed by Garrett and Cummins (2007). They found out that turbines in a fence benefit from local blockage effects if they are working at their optimal operating point. Vogel and Willden (2017, 2019) used a BEM model with the forces and power production adapting to several tested advance parameters. They found out a maximal power production increase of 26% for a fence of eight machines compared to the power production of the same isolated machines in free-stream conditions, with a mean power coefficient  $C_p=0.608$  instead of 0.484. Dominguez et al. (2016) considered 2D fences of ducted cross-flow water turbines. A power increase factor equal to 2.6 was found for a fence containing 15 turbines with a lateral spacing of 1 turbine width and a blockage ratio of 0.4. More recently an experimental study (McNaughton et al., 2019) showed that two side-by-side axial turbines witness a power production increase if they are placed close to each other and operate at their new optimal advance parameter. Concerning staggered configurations, the URANS farm simulation realized by Nuernberg and Tao (2018) showed a small increase of the production of turbines placed closely downstream and on the side of a first one, with a maximum 11% power increase. Ordonez-Sanchez et al. (2017) did experi-

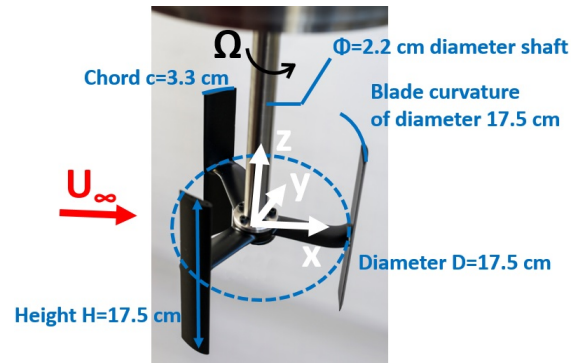


**Figure 1:** Reduced-scale Darrieus turbine tested and modeled in the simulations

mental measurements for different configurations of cross-flow turbine arrays and also found power increases when adapting the turbine advance parameters.

The present study aims at developing a 3D steady-state method for turbine array modelings that does not need aerodynamic foil coefficients nor empirical data for taking into account the rotating blades and the possible stall phenomena. Moreover, the proposed method allows one to calculate the turbine power production with a good accuracy, and different farm configurations are tested. The turbine used is a three-bladed ( $n=3$ ) reduced-scale Darrieus turbine, that had already been experimented by Maître et al. (2013). Its characteristics are presented in Figure 1. It has a diameter  $D=175$  mm and a height  $H=175$  mm. The blades are NACA0018 profiles, with a camber following a rotating circle of diameter 175 mm. Its chord value is  $c=32$  mm, leading to a solidity  $2nc/D=1.1$ . The upstream flow direction is represented by the vector  $U_\infty$ , and the rotational speed  $\Omega$  is controlled. The turbine advance parameter is defined in a classical way as  $\lambda = \Omega D / (2U_\infty)$ . The origin of all coordinates in this work is the intersection of the rotation axis and the mid-height plane of the turbine. The  $x$  axis is along the inlet flow direction,  $z$  is the vertical axis and  $y$  the transverse axis.

The force distributions used are obtained from a few unsteady RANS rotor-stator simulations of the turbine done for different upstream flow conditions. An interpolation from those force distributions is performed for intermediate cases. The model developed adapts the force values to the upstream flow velocity, with an equation linking those forces to the local velocity calculated for each turbine. Therefore simulations of any configuration of turbine array can be easily performed without having to tune any parameter. The method can be extended to axial turbine or others. In any case the mesh used is cartesian, which will be an advantage in the future to calculate the influence of the masts or external parts of the turbine not represented in this study. Those parts could be modeled by adding the corresponding drag force in the affected cells, or by the use of IBM methods that prove to be efficient on cartesian meshes (Constant et al., 2017).

## 2. Methodology

### 2.1. Preliminary URANS simulations

The force distributions imposed in the adaptive model are results obtained beforehand from unsteady blade-resolved simulations of the Darrieus turbine. These simulations are done with the open source software OpenFoam4.1. A RANS turbulence closure model is used with the k-Omega Shear Stress Transport linear eddy viscosity equations (Menter, 1994; Menter et al., 2003). This model has two equations on  $k$  and  $\omega$ , and allows to capture correctly the flow separation. It has been widely used to calculate the performances and loads of cross-flow turbines. Maître et al. (2013) used this turbulence model and did a mesh sensitivity analysis for a 2D simulation of a Darrieus turbine. To capture the boundary layer flow near the turbine, they found out that the maximum dimensionless wall distance  $y^+$  has to be lower than 5 (with good results obtained for values always lower than 2), and the mean  $y^+$  value has to be less than 1. Kramer et al. (2015) showed that a 3D URANS simulation with a mean  $y^+$  value less than 1 is able to reproduce correctly the geometry effects like the arm-blade connections. In our simulations, the wall refinement used has a cell height of  $1.0 \times 10^{-5}$  m near the wall and is extended within 15 layers, with a growth rate of 1.17. After convergence, a maximum  $y^+$  value of 2.4 and a mean value always lower than 0.2 are obtained for the different positions during one turbine revolution and for all the simulated advance parameters. The inlet conditions are a flow velocity of 2.3 m/s, a turbulence intensity of 2.5%, and a value  $\omega = 1 \text{ s}^{-1}$ , which is low and creates no turbulence decay along the domain. Wall laws are used as lateral, top and bottom boundary conditions. The outlet conditions are a constant pressure condition and a zero gradient velocity condition. The dimensions of the simulation domain are 0.60 m wide, 0.55 m high and 2.5 m long in the direction of the flow (0.5 m upstream, and 2 m downstream of the turbine). A view of this domain is presented in Figure 2. To reduce the number of cells, a symmetry is used on the median plane ( $z=0$ ), therefore only the upper half of the domain in Figure 2 is simulated. The turbine rotation is taken into account using a dynamic mesh interface between the tunnel domain and a cylinder containing the turbine. These specifics lead to a full mesh composed of about 14 million cells, with 9 million cells in the rotor domain. The turbine shaft and its support structures are not modeled.

The pimpleDyMFoam solver is used to get accurate results in acceptable time. It is a large time-step transient solver for incompressible, turbulent flow, using the PIMPLE (merged PISO-SIMPLE) algorithm. It is able to take into account dynamic meshes. The numerical schemes used are second order (backward) for the time, and second order for pressure, velocity,  $k$  and  $\omega$  (Gauss linear) with a limiter for  $k$  and  $\omega$ . Classical time step values are used, depending on the advance parameter  $\lambda$  simulated for the turbine. At  $\lambda \geq 2$ , which is larger or close to the optimal advance parameter in the present study, the time step is chosen to correspond to a rotation of the turbine of 1 degree. This value was recom-

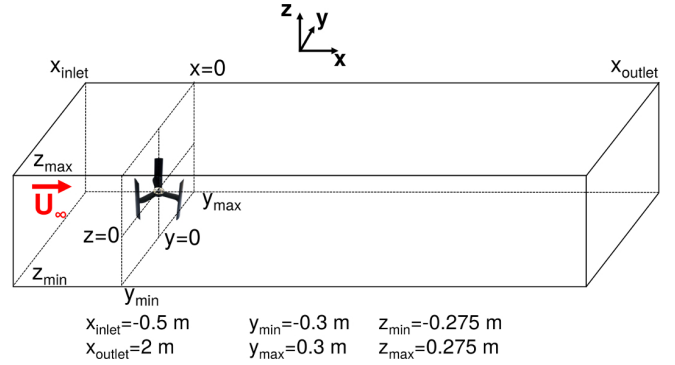


**Figure 2:** View of the domain and the turbine position in the simulations. The turbine center ( $x=y=z=0$ ) corresponds to the middle of the section

mended by Maître et al. (2013). A smaller time step corresponding to 0.5 degree of rotation is chosen for lower  $\lambda$  values. A maximum of 30 subiterations is chosen for each time step. Results are obtained only once the two following criteria are met: at least 12 revolutions of the turbine have been completed, and the flow is converged in the wake. Doing only 6 revolutions has led to differences with the final force and power values less than 1%. Using a coarser mesh containing 6 million cells with the same near wall grid has also led to differences of the same order of magnitude.

The URANS simulation results are compared to experiments using the same reduced-scale Darrieus turbine. New experiments were conducted in the CERG hydrodynamic tunnel TH2 in Grenoble, whose test section is approximately 2 m long with a constant rectangular shape that is 60 cm wide by 55 cm high. Three different flow velocities are used in the test section: 1.8 m/s, 2.3 m/s and 2.8 m/s. The turbine is not centered and is shifted 5 cm towards negative  $y$  values, but simulations showed that this has no influence since the walls are far enough away from the turbine.

A turbulence grid is located 1 m upstream of the turbine, and creates homogeneous isotropic turbulence. It has rectangular bars of thickness 1 cm regularly spaced each 5 cm in the two transverse directions. The turbulence intensity has been measured beforehand without turbine along the tunnel, and an extrapolation at the turbine location (where the absence of window is hindering measurements) gives the turbulence intensity value of 5.5%. This value is different from the URANS inlet turbulence intensity value, but no significant effect is expected because the flow through vertical axis turbines has a low sensitivity to turbulence. Three different flow velocities have been tested. The instrumentation of the turbine is detailed in the work of Maître et al. (2013).

The power production of the turbine is measured via the electrical torque, and the corresponding power coefficient  $C_p$  is deduced.  $C_p$  is equal to the turbine kinetic power  $P$  divided by the maximum extractable power from a free stream flow of velocity  $U_\infty$ , considering the projected section  $S$  of

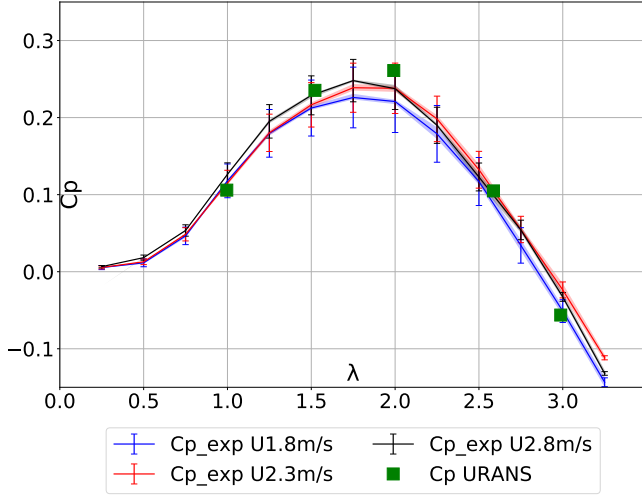


**Figure 3:** Comparison of the experimental and URANS blade-resolved simulation  $C_p$  curves

the turbine:

$$C_p = \frac{P}{1/2\rho S U_\infty^3} \quad (1)$$

In this equation,  $\rho$  is the density of the water, chosen to  $1000 \text{ kg/m}^3$ . The  $C_p$  curves for each flow velocity are compared to the numerical  $C_p$  values obtained with the URANS blade-resolved simulation of the turbine in Figure 3. All experimental curves are close which means that there are few Reynolds effects for those tunnel velocities. The URANS curve is in good agreement with the experimental ones, with the highest error for  $\lambda = 2$ .

Forces along the streamwise ( $x$ ) and lateral ( $y$ ) directions are measured via piezoelectric sensors, and the corresponding dimensionless force coefficients  $C_x$  and  $C_y$  are deduced. In order to compare them with the results of the URANS blade-resolved simulation that was done without the turbine shaft, the drag created by this part is estimated using the drag coefficient curve of an infinite fixed cylinder of the same diameter. The value of  $12.3 \text{ N}$  is calculated and is added to the total simulated drag. The comparison of the experimental and simulation results is presented in Figure 4. The  $C_x$  results are very close, but there are discrepancies in term of  $C_y$  values, with high relative errors since the turbine transverse force values are small. However the URANS simulation is validated against the experiments and its results are used to construct the simplified model as explained in the following section.

## 2.2. A force conservative simplified model

In our simplified model, a classical representation of the turbine is used: force source terms are added in the momentum equations for each cell of the domain swept by the turbine. The method used to obtain a time-averaged force field from the URANS simulation results consists of two steps. The first step is to project the forces on a new cylindrical

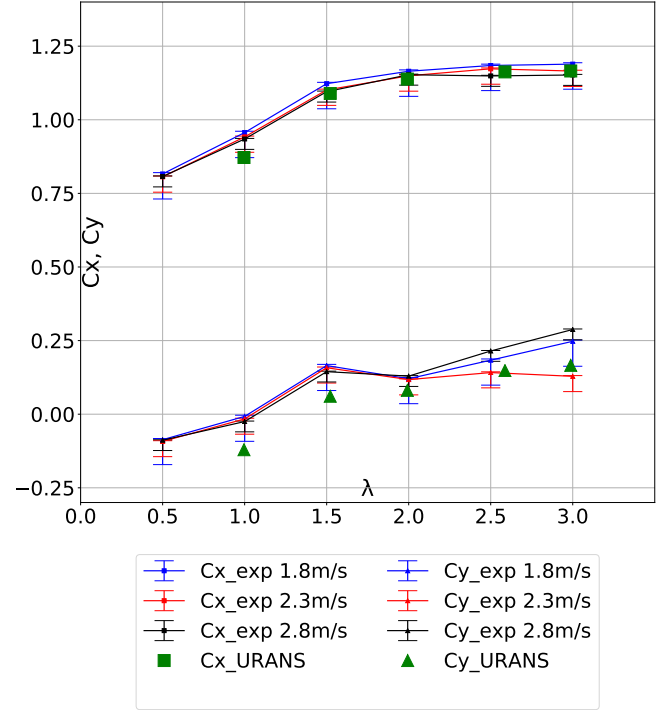


**Figure 4:** Comparison of the experimental and URANS blade-resolved simulation  $C_x$  and  $C_y$  curves

mesh, which geometry is adapted to represent the Darrieus force distribution. It is more suitable than using a cartesian mesh that might lead to a loss of information if the mesh is too rough, or to discontinuities if the cell sizes are too close to the URANS cell dimensions. The cylindrical mesh used is presented in Figure 5. Its cells are the basic volume elements of a fixed cylindrical coordinate system ( $O, r, \theta, z$ ), which does not rotate with the turbine. The decomposition is done here for the half of the turbine simulated, and will be extended later by symmetry to the whole turbine. The zone where blade forces are present is decomposed into one cell in the radial direction  $r$ , 10 cells in the  $z$ -direction and 72 cells along the  $360^\circ$  of  $\theta$  ( $d\theta = 5^\circ$ ). The arm forces are extracted in a domain that contains 10 cells in the radial direction and 1 cell in  $z$ -direction, with  $d\theta = 5^\circ$ . When the simulation is converged, during one turbine revolution, both arm and blade forces are extracted for each cell of this cylindrical mesh, for each time step equivalent to  $1^\circ$  or  $0.5^\circ$  of rotation. This referential being fixed, at each time step, cells of the cylindrical mesh intersect either a part of the blades or arms (in this case the corresponding forces are extracted) or only a fluid part (no forces are extracted). At last, a time-averaging of those force distributions during the whole turbine revolution is performed for each cell to obtain a steady-state spatial distribution of the forces.

The second step is a projection of those forces on a new cartesian mesh, of which the cell size can be adapted to have a proper representation of the turbine. This projection step has been chosen for its simplicity to model whatever number of turbines in an array without having to take care of

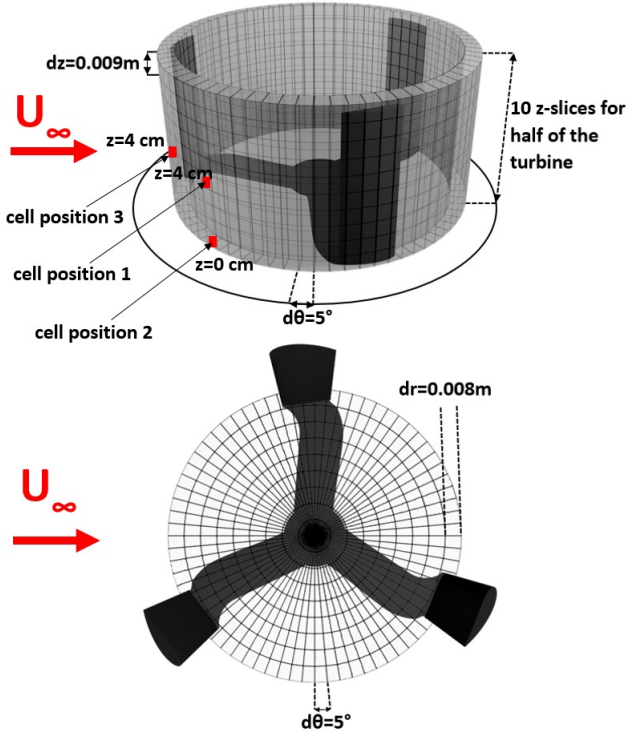


**Figure 5:** Cylindrical mesh used to compute the time-averaged forces to be used in the Actuator model simulations, with the blade domain mesh on the top and the arm domain mesh on the bottom. The monitoring cells used in this work are presented in red

the turbine positions to construct the mesh. Forces from the cylindrical steady-state force distribution are projected in the simplified model mesh. The cell forces imposed in the simplified mesh are obtained from a weighting of the forces of all the neighbor cells of the cylindrical mesh whose center is comprised within a distance lower than a constant distance of the code, named  $dist\_action$ . This is illustrated in Figure 6 for a two dimension mesh. In the following equations, the index  $i$  is taken for numbering the cells of the simplified mesh (noted  $Mesh_{simp.}$ ), and the index  $j$  for cells of the cylindrical mesh (noted  $Mesh_{cyl.}$ ).  $\gamma_{ij}$  is a linear function of the distance  $dist_{ij}$  between the cells  $i$  and  $j$ , and is defined as:

$$\gamma_{ij} = dist\_action - dist_{ij} \quad \text{if} \quad dist_{ij} \leq dist\_action \quad (2)$$

$$\gamma_{ij} = 0 \quad \text{if} \quad dist_{ij} > dist\_action \quad (3)$$

In order to have the conservation of the total forces applied in the mesh, a factor has to be used to calculate the part of the force on a cell  $i$  due to the influence of the cell  $j$ . It is the function  $\beta_{ij}$  calculated as:

$$\beta_{ij} = \frac{\gamma_{ij}}{\sum_{k \in Mesh_{simp.}} \gamma_{kj}} \quad (4)$$

The total force vector  $F_i$  applied on the cell  $i$  of the simplified mesh is defined as a function of the cylindrical mesh

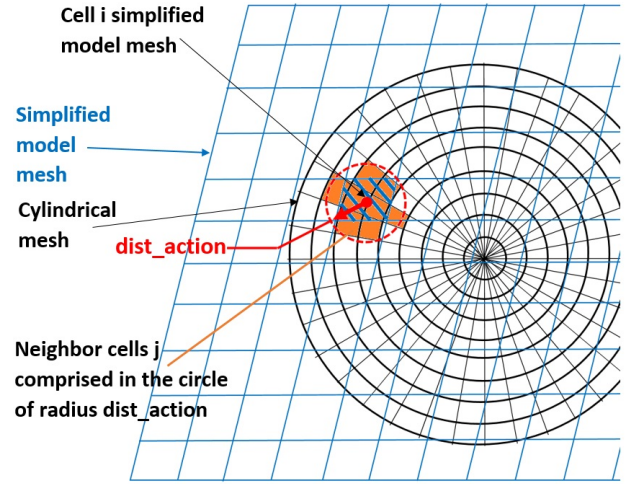


**Figure 6:** 2D view of the force projection: the orange cells are all the neighbor cells  $j$  of the cylindrical mesh used to get the force applied on the cell  $i$  of the simplified model mesh

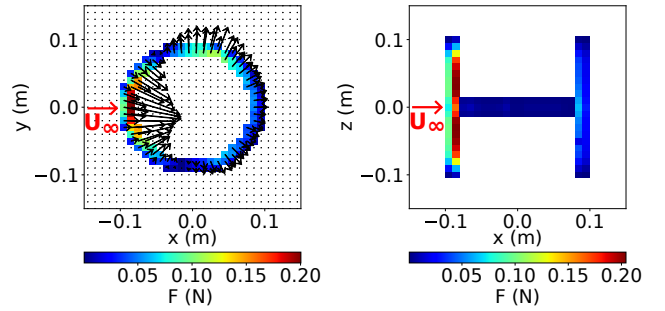


**Figure 7:** View in the horizontal plane  $z=-2$  cm ( $z/R=-0.23$ ) (left) and the vertical plane  $y=0$  (right) of the turbine forces applied on each cell of the adaptive model

cell forces  $f_j$ , as:

$$F_i = \sum_{j \in Mesh_{cyl.}} f_j \beta_{ij} = \sum_{j \in Mesh_{cyl.}} \frac{f_j \times \gamma_{ij}}{\sum_{k \in Mesh_{simp.}} \gamma_{kj}} \quad (5)$$

It can be easily seen that the addition of the forces  $F_i$  for all cells of the simplified mesh is equal to the total force applied on the cylindrical mesh. Another advantage of this method is that a smoothing is automatically done close to the borders of the turbine area. Indeed, even if cells are not comprised in the turbine swept volume, they witness a force contribution from cells comprised in a distance  $dist\_action$ . The factor  $dist\_action$  is therefore a smoothing factor of our simulations that has to be chosen carefully.

The force distribution obtained after projection for  $\lambda = 2$  is presented in Figure 7 in the horizontal plane  $z=-2$  cm ( $z/R=-0.23$ ) (under the turbine arms), and the vertical plane  $y=0$ .

A grid sensitivity study has been done. It is linked to the smoothing parameter  $dist\_action$  presented before, and both the cell size  $dx$  and this parameter have been tested. In order to be sure to have at least one cell in the radius direction for

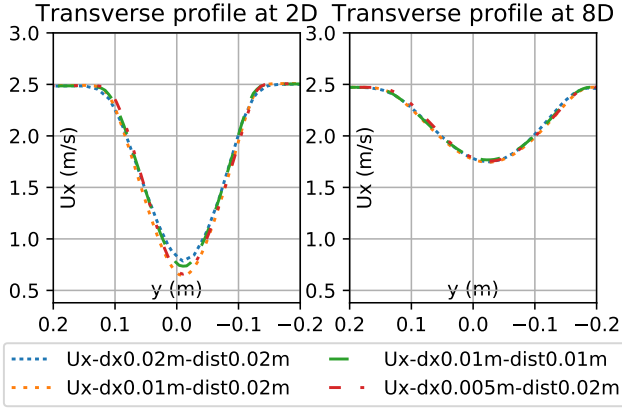


**Figure 8:** Velocity profiles 2D and 8D downstream of the turbine for the different cell sizes  $dx$  and  $dist\_action$  tested

modeling the blades, the parameter  $dist\_action$  can not be lower than  $dx$ . The velocity deficits at 2 diameters (2D) and 8 diameters (8D) downstream of the turbine are plotted versus  $y$  at the altitude  $z=-2$  cm, for different values of the tested parameters. They are presented in Figure 8. We observe that the curves are converging towards the curve with  $dx=0.005$  m. The case with  $dx=0.01$  m and  $dist\_action=0.02$  m gives the same velocity profiles and it will be used in the simulations. It gives better results than using  $dist\_action=0.01$  m, because in this last case the arms are badly represented with only one cell in the  $z$ -direction and no vertical forces imposed, and the near-wake is slightly impacted. The chosen parameters  $dx=0.01$  m and  $dist\_action=0.02$  m lead to a small over estimation of the turbine drag and power of respectively 2.4% and 3.6% compared to the converged values.

### 2.3. Research of a maximum efficiency operating point independent of the confinement

A classical representation of the turbine performances is the power coefficient versus  $\lambda$  curve, already presented in Figure 3. This curve presents a maximum of efficiency for  $\lambda$  close to 2, and can be used to calculate the turbine power production in free stream conditions knowing the upstream flow velocity  $U_\infty$ . With a turbine placed in a restricted section, for example in a natural channel or between other turbines in an array, the flow just upstream of the turbine is generally accelerated compared to an isolated configuration. This effect is due to the straightening of the streamlines upstream the turbine. It induces an increase of the turbine extractable power. As a consequence, the power production can not be calculated with the performance coefficient of equation 1 anymore.

The confinement number is usually defined as  $S/S_{channel}$ , with  $S_{channel}$  the cross section of the channel simulated. In the present simulations, the domain height is kept constant and the confinement is changed in the horizontal direction, to correspond to turbines close to each other always located at the same water depth. A lateral confinement is defined as  $\epsilon = D/b$ , with  $D$  the turbine diameter and  $b$  the horizontal

dimension of the channel chosen for each simulation.

Three different confinement geometries are simulated with the URANS model:  $\epsilon=0.29$ ,  $\epsilon=0.44$ , and  $\epsilon=0.58$ . Different advance parameters are used to draw the power coefficient curves. For each simulation, a mean local velocity  $U_{local}$  is calculated to obtain a new local advance parameter  $\lambda^*$ , defined as:

$$\lambda^* = \Omega D / (2U_{local}) \quad (6)$$

The local velocity is calculated as the mean streamwise velocity value in all cells of the cylinder swept by the vertical axis turbine, that is time-averaged over one turbine revolution.

The local power coefficient  $Cp^*$  is defined using the local velocity instead of the free stream velocity, as:

$$Cp^* = \frac{P}{1/2\rho S U_{local}^3} \quad (7)$$

The local force coefficients for each components of forces (the local thrust coefficient  $Cx^*$  and the equivalent coefficients in the 2 other directions  $Cy^*$  and  $Cz^*$ ) are defined in the same way, using the local velocity instead of the free stream velocity, and depending on the three components of the total forces applied on the turbine  $F_{x,y,z}$ :

$$C_{x,y,z}^* = \frac{F_{x,y,z}}{1/2\rho S U_{local}^2} \quad (8)$$

The  $Cp$  versus  $\lambda$  curves are presented for each confinement in Figure 9.a, and compared to the corresponding  $Cp^*$  versus  $\lambda^*$  curves in Figure 9.b. The labels added on this last plot correspond to the respective  $\lambda$  values used for each calculation point. The  $Cp$  versus  $\lambda$  curves are different for each confinement, and the maximum efficiency values are increasing as the confinement is increasing. The maximum of efficiency is also slightly shifted towards larger  $\lambda$  values as the confinement is raised. However the  $Cp^*$  versus  $\lambda^*$  curves are all superimposed. A 4<sup>th</sup> order polynomial fitting curve has been drawn, using the method of least squares with all the  $Cp^*$  calculated points. All points are very close to the fitting curve, in regard to the simulation uncertainties. A justification is proposed for the existence of this unique curve. The turbine performances are increased if the velocity triangles on its blades are favorable. It means that the angle of attack on the blades has to be optimized. This angle depends on the relative velocity, and the  $\lambda^*$  parameter is a good spatial average representation of this velocity for the whole turbine volume. Therefore a same  $\lambda^*$  parameter leads approximately to the same power coefficient.

The classical and local force coefficients on the  $x$  and  $y$  axes are drawn in Figures 10 and 11. The force values in the  $z$ -direction are not presented. 4<sup>th</sup> order polynomial fitting curves have been plotted using all the simulated  $Cx^*$  and  $Cy^*$  points. The dimensionless local force coefficients are also independent from the confinement in Figures 10.b and 11.b.

Finally, time-averaged force values at several turbine locations have been monitored in the cylindrical mesh. The chosen locations are shown in Figure 5. The positions 1 and 2 are located in the zone of strong radial and tangential forces, at the angle  $\theta=207.5^\circ$ . Position 1 is at the turbine center altitude ( $z=0$ ), and position 2 is located at  $z/R=0.46$  where there is no influence of the arms. Position 3 is located at  $z/R=0.46$ , at the most upstream position of the turbine ( $\theta$  close to  $180^\circ$ ). The cell forces for those monitored cells are also made dimensionless using the local velocity to get the coefficients  $cx, y, z_{cell}^*$ . The values  $cx_{cell}^*$  and  $cy_{cell}^*$  are plotted versus  $\lambda^*$  for the three different confinement configurations in Figure 12. Only three  $\lambda$  values have been simulated. The piecewise linear curves are drawn with the three points obtained for the confinement case  $\epsilon = 0.29$ . For each position, the points obtained for the other confinement cases are located on these curves, even if small discrepancies occur. The monitoring on all the other cells gives the same order of accuracy. Excepted the calculation uncertainties, a source of discrepancies can be the fact that the mean local velocity over the whole Darrieus turbine is used, and forces can be locally slightly different for some confinement cases if the flow velocity and angle of attack are locally modified, for example by the presence of nearby channel walls. However, it is shown that those dimensionless force coefficients obtained for each cell of the cylindrical mesh are also independent from the confinement. They will be used later in the adaptive model without any additional confinement correction.

Each  $C_p$  versus  $\lambda$  curve in Figure 9.a has a different point of maximum efficiency. Those points are found using the different polynomial fitting curves. For each confinement, the order of the fitting polynomial is the number of simulated points minus one. The corresponding  $C_p^*$  and  $\lambda^*$  are calculated and presented in Table 1. It appears that the  $C_p^*$  and  $\lambda^*$  values found are close to each others. Taking the average of those points is a good approximation of a maximum efficiency operating point, independent from confinement. The maximum differences in terms of  $\lambda^*$  and  $C_p^*$  between two points are noted respectively  $\Delta\lambda^*$  and  $\Delta C_p^*$ . The uncertainty analysis for the maximum power output  $P_{max}$  is done as following:

$$P_{max} = 1/2\rho S U_{local}^3 C_p^* = \frac{\rho S (\Omega D/2)^3 C_p^*}{2\lambda^{*3}} \quad (9)$$

$$\implies \frac{\Delta P_{max}}{P_{max}} = -3 \frac{\Delta\lambda^*}{\lambda^*} + \frac{\Delta C_p^*}{C_p^*} \quad (10)$$

By using values found in Table 1, the relative error  $\Delta C_p^*/C_p^*$  is lower than 2.7% and the relative error  $\Delta\lambda^*/\lambda^*$  lower than 3%, which gives a total error on the maximum power production always lower than 11.7%. Therefore, using  $\lambda^*=3.6$  and  $C_p^*=1.98$  is a good approximation for imposing the best efficiency operating point in the simulations, for any possible flow configuration.

**Table 1**

Interpolated local parameters corresponding to the points of maximum efficiency for the 3 confinement cases

$\epsilon_{lat}$	$\lambda$	$C_p$	$U_{local}$	$\lambda^*$	$C_p^*$
$\epsilon_{lat} = 0,29$	1.825	0.273	1.19	3.53	1.932
$\epsilon_{lat} = 0,44$	1.925	0.301	1.23	3.61	1.982
$\epsilon_{lat} = 0,58$	2.05	0.341	1.27	3.70	2.036

## 2.4. The adaptive model implementation

In real operating cases, the turbine performances and the forces applied on the turbine depend on the configuration of the flow through the turbine. The aim here is to develop an adaptive model that calculates automatically the forces and performances depending on this flow using the  $\lambda^*$  parameter.

The calculation loop steps for the so-called adaptive model are summarized in Figure 13. Dimensionless URANS force distributions (the  $cx_{cell}^*$  and  $cy_{cell}^*$  distributions from Figure 12, and the corresponding  $cz_{cell}^*$ ) have been extracted on the cylindrical mesh for three  $\lambda^*$  values: 1.4, 4.25 and 9.7. A linear interpolation is done for each cell if the chosen  $\lambda^*$  is located in-between those values. The force coefficients are then multiplied by the term  $1/2\rho S U_{local}^2$  to get the force distributions that will be projected on the cartesian mesh, according to the previous paragraph. Those forces are added in the Navier-Stokes equations, then the flow and the new local velocity are calculated for the current iteration. After convergence, the final  $U_{local}$  value is calculated and the  $C_p^*$  versus  $\lambda^*$  curve of Figure 9.b is used to calculate the corresponding power production of the turbine.

The adaptive model is tested for different configurations: for the CERG test case in next section, and for array calculations in section 4. The CERG test case simulation is performed as a model validation. The adaptive model in which the force distribution is an unknown is compared with the force conservation model using the forces given by the URANS calculations. Moreover a 2D version of these two models removing the z-direction has been implemented to measure the effect of the 2D assumption on the results. The same software and setup are used (and the same cell size  $dx=dy=0.01$  m in the central zone). The only differences are the domain size which is modified to keep the same turbine confinement, and the force distribution which is adapted in 2D. The confinement in 3D is  $DH/(bh) = 0.0928$ . In 2D, the value  $b=188.6$  cm is chosen to have the same confinement value  $D/b = 0.0928$ . The z-component of force vanishes in 2D. Because the turbine height is set equal to  $H$ :

$$F_{x,y}^{2D}(r, \theta) = \sum_{z_k=z_k^{min}}^{z_k^{max}} \frac{F_{x,y}^{3D}(r, \theta, z_k)}{H} \quad (11)$$

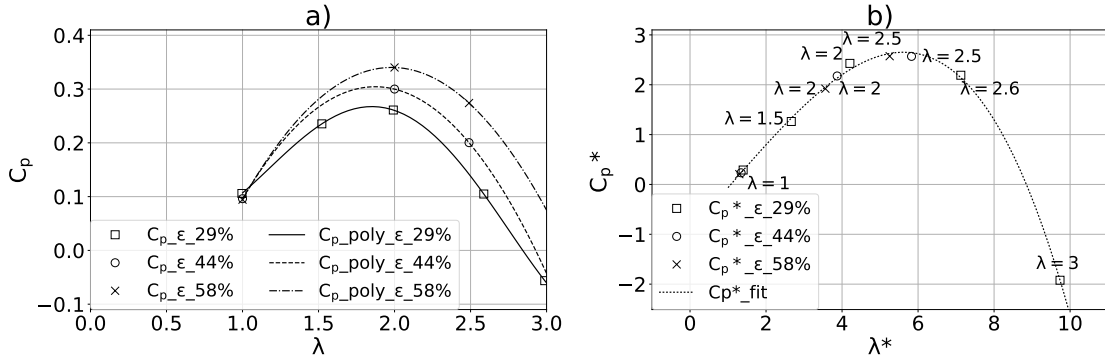


Figure 9: a)  $C_p$  versus  $\lambda$  curve and b)  $C_p^*$  versus  $\lambda^*$  for the three confinement cases

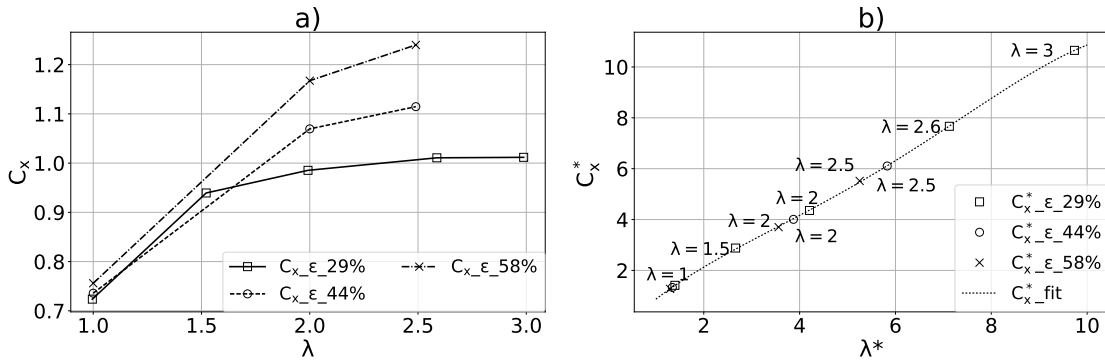


Figure 10: a)  $C_x$  versus  $\lambda$  curve and b)  $C_x^*$  versus  $\lambda^*$  for the three confinement cases

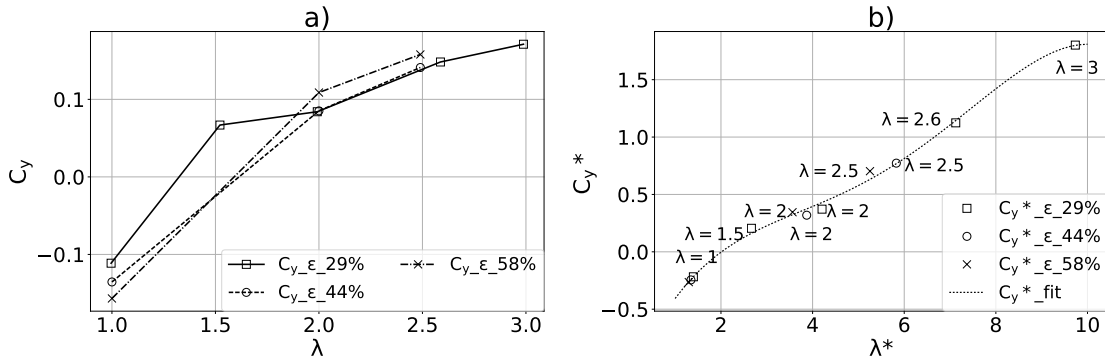


Figure 11: a)  $C_y$  versus  $\lambda$  curve and b)  $C_y^*$  versus  $\lambda^*$  for the three confinement cases

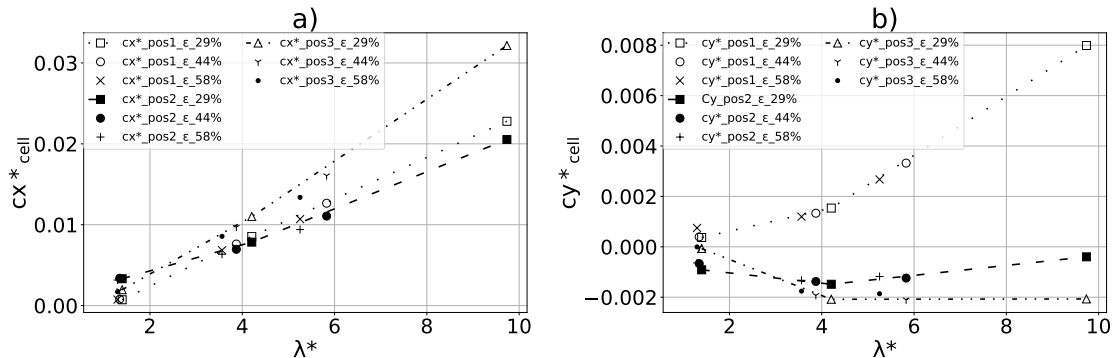


Figure 12: a)  $c_x^*$  versus  $\lambda$  and b)  $c_y^*$  versus  $\lambda^*$  for the three confinement cases and the three monitored positions of Figure 5

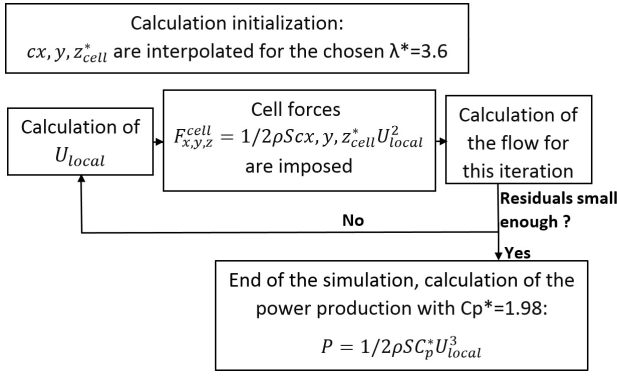


Figure 13: Computation loop of the adaptive model

In the case of array calculations, the low array confinement is enough to have no influence on the results anymore, therefore the same  $x$  and  $y$ -domain lengths are used both in the 2D and 3D models.

### 3. Simulation results for a single machine

#### 3.1. The test-case setup

To check the validity of the simulation results, PIV measurements have been realized on the experimental hydrodynamic tunnel downstream of the turbine, in several horizontal planes of different altitudes. The reference plane is located at the altitude  $z=1$  cm, then 5 planes are located above it and 5 planes below it. Each of the consecutive planes are separated by a 4 cm increment in the  $z$ -direction. Vertical profiles of the axial velocity are reconstructed at several  $x$ -positions downstream of the axis of the turbine with the values obtained on the horizontal planes. The experimental values present a shift of approximately 3 cm towards the top of the tunnel compared to the simulations. It has been observed that the peculiar geometry of the flume with an upstream half-convergent section placed only in the lower part of the tunnel creates a  $z$ -component of velocity close to 0.05 m/s. This deviates progressively the wake of the turbine towards the top. Hence all measurement points altitudes are shifted of -3 cm when compared to the numerical results. The reference plane will therefore be described as the plane of altitude  $z=-2$  cm when compared to numerical results.

The simulation domain is the domain already presented in Figure 2, that corresponds to the experimental setup. The  $k$ -Omega Shear Stress Transport turbulence model is used. The uniform inlet velocity of 2.3 m/s is chosen, and the turbulence inlet values are chosen to  $k = 0.0711 \text{ m}^2/\text{s}^2$  and  $\omega = 90 \text{ s}^{-1}$  in order to have the turbulence intensity value of 5.5 % and the correct turbulence decay at the turbine location.

#### 3.2. Wake results

The advance parameter  $\lambda = 2$  is first simulated with all models. It is slightly different from the point of maximum efficiency presented in Table 1. The corresponding forces calculated via the URANS simulation are imposed for the

force-conservation model, and  $\lambda^* = 4.25$  is now imposed in the adaptive model, that was the local advance parameter calculated in the URANS simulation at  $\lambda = 2$ . The wakes obtained are compared to the experimental one. The transverse velocity profiles are plotted in Figure 14 in the horizontal plane of altitude  $z=-2$  cm ( $z/R=0.23$ ), at several positions downstream of the turbine (at the distances  $2D, 3D, \dots$  downstream of the turbine axis). The available vertical velocity profiles are plotted at the same positions downstream of the turbine in Figure 15, at the lateral position  $y=0$  cm. We observe that both 3D models give sensibly the same results, even if the forces imposed are slightly different: the turbine drags are respectively equal to 80,2N and 84,3N for the force-constant and the adaptive cases though the experimental drag without the axis drag is equal to 79,9N. The velocity in the wake is indeed little sensitive to the imposed force values. Regarding the vertical profiles, results are more accurate in the lower part where the shaft of the turbine is not present in the experiments, than in the upper part where the shaft is present in the experiments but not in the simulations. In both Figures, the 3D simulation results are in good agreement with the experiments in the far-wake, at distances larger or equal to  $4D$  or  $6D$ . There are discrepancies in the near-wake, that are common with the use of Actuator force models. The eddies generated by the turbine blades are not calculated with those models but may influence the velocity field in the near-wake. Therefore we can not expect to have accurate predictions in the near-wake, but the model is validated for modeling turbine arrays with distances higher than  $4D$  between consecutive turbines.

The turbulent kinetic energy ( $k$ ) profiles are also plotted at the same positions in the horizontal plane of altitude  $z=-2$  cm, in Figure 16. The differences found between the two models are insufficient to act on the velocity profiles. The turbulent kinetic energy is over-estimated in both simplified models compared to the experiments. It causes the wake to decay fast enough, which was not the case for axial turbine in classical Actuator Disk models for which authors tried to add extra turbulence source terms at the disk position (Nguyen et al., 2016). Our vertical axis Actuator force model creates this extra turbulent kinetic energy by itself, which makes the velocity recover fast enough in the wake.

Regarding the horizontal profiles obtained with the 2D simulations, the velocity deficit does not decrease fast enough and there are big discrepancies in the far-wake. In the turbulence theory (Pope, 2000), the velocity deficit decay of an axisymmetric wake as a function of the position  $x$  is following the function  $x^{-2/3}$  in 3D, whereas it is following the function  $x^{-1/2}$  in 2D that decreases slower. This is due to geometrical aspects, as the wake limits where the mixing occurs are an area circling the wake in 3D, and only two lines in both sides of the wake in 2D. Therefore 2D models are not expected to give correct results for the wake prediction without adding any extra correcting force or turbulence source term.

However 2D models require much smaller calculation efforts. To quantify the discrepancies that can be introduced by these models, the 2D version of the developed model has

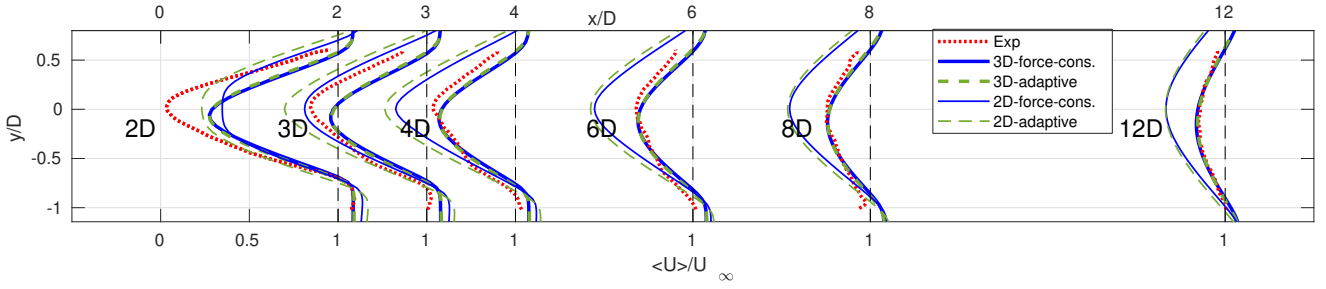


**Figure 14:** Transverse velocity profiles for each model and the experiment at several positions  $x/D$  downstream of the turbine, in the horizontal plane of altitude  $z=-2$  cm ( $z/R=-0.23$ )

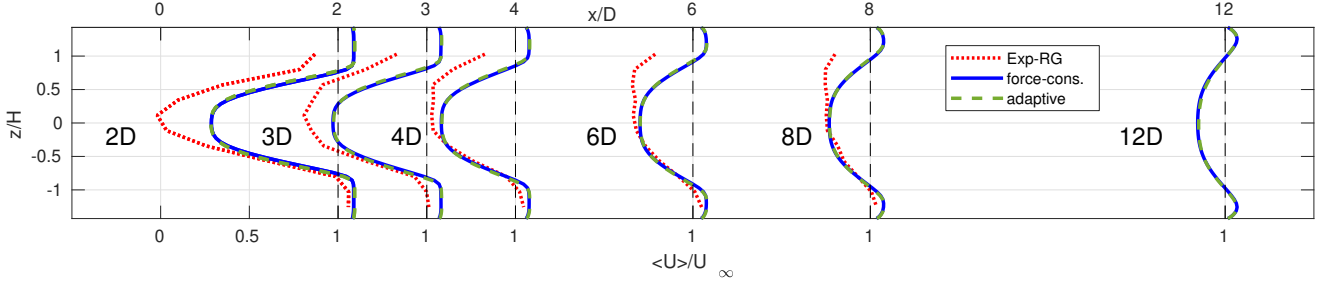


**Figure 15:** Vertical velocity profiles for each model and the experiment at several positions  $x/D$  downstream of the turbine, in the vertical plane  $y=0$  cm

been compared to the 3D one in terms of power production and velocity deficits, in the next sections.

### 3.3. Power production results

The force conservation model results are presented for the cases  $\lambda = 1$ ,  $\lambda = 2$  and  $\lambda = 3$ , as well as the corresponding adaptive model results for  $\lambda^* = 1.4$ ,  $\lambda^* = 4.25$  and  $\lambda^* = 9.7$ . The Table 2 summarizes the experimental, URANS, and the two aforementioned models results with the calculated local velocity,  $\lambda$ ,  $\lambda^*$ ,  $C_p^*$ , power (P) and relative error on power (Er. P). The URANS simulation is taken as reference because its force values are used rather than the experimental ones in the two Actuator force models.

For the case  $\lambda = 2$  (close to the optimal advance parameter), both 2D models present high power production discrepancies and are not accurate for calculating this value. In 3D as well as in 2D, results are more accurate for the adaptive model. The local velocity calculated is closer to the URANS

calculated one. The power production is hence better calculated, with errors of 3.5% (14.3% in 2D) for the adaptive model and 21.5% (56.4% in 2D) for the force conservation model. The larger error value obtained with the force conservation model is due to an overestimation of the local velocity leading to an overestimation of the power using equation 7. The force conservation approach is the classical approach and implies a conservation of the total forces. But this approach might not be the best to model the flow through the turbine and its wake. Another approach would be to enforce the flow rate through the turbine, which might create a more accurate wake in the simulation. The adaptive model is a compromise between those two approaches. In this model, neither the force values nor the local velocity  $U_{local}$  are conserved, but the  $\lambda^*$  value is imposed. It gives a relation linking the local velocity and the forces imposed, that leads to a compromise between the conservation of those two values.

For the lower advance parameter  $\lambda = 1$ , corresponding

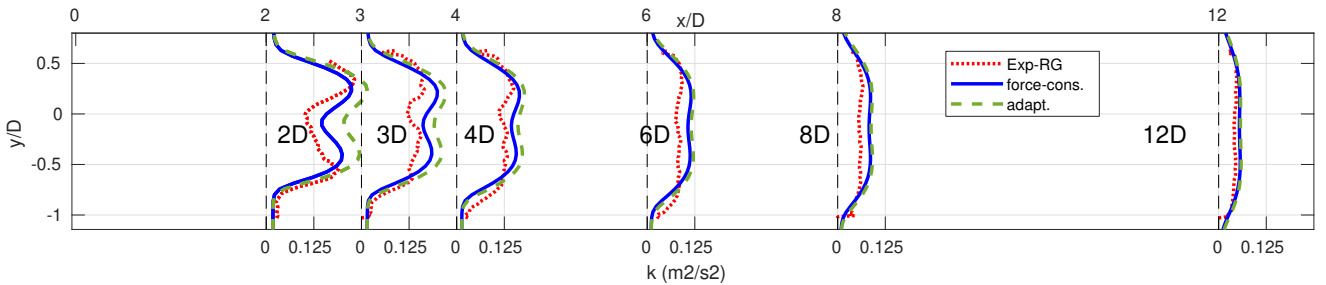


**Figure 16:** Transverse turbulent kinetic energy profiles for each model and the experiment at several positions  $x/D$  downstream of the turbine, in the horizontal plane of altitude  $z=-2$  cm ( $z/R=-0.23$ )

**Table 2**

Comparison of the main criteria for the experiments, the URANS simulation and the two Actuator force models for three advance parameters

Model	$\lambda = 2$	$U_{local}$	$\lambda$	$\lambda^*$	$C_p^*$	P (W)	Er. P
URANS (ref)	1.094	2	4.25	2.32	48.9	—	
Experiment	—	2	—	—	44.3	-9.4%	
for.-cons. 3D	1.239	2	3.71	2.04	59.4	21.5%	
adaptive 3D	1.125	2.08	4.25	2.32	50.6	3.5%	
for.-cons. 2D	1.421	2	3.24	1.75	76.5	56.4%	
adaptive 2D	1.163	2.15	4.25	2.32	55.9	14.3%	
Model	$\lambda = 1$	$U_{local}$	$\lambda$	$\lambda^*$	$C_p^*$	P (W)	Er. P
URANS (ref)	1.644	1	1.4	0.29	19.7	—	
Experiment	—	1	—	—	21.4	8.6%	
for.-cons. 3D	1.657	1	1.4	0.29	18.8	-4.6%	
adaptive 3D	1.649	1.01	1.4	0.29	19.9	1.0%	
Model	$\lambda = 3$	$U_{local}$	$\lambda$	$\lambda^*$	$C_p^*$	P (W)	Er. P
URANS (ref)	0.709	3	9.7	-1.92	-10.5	—	
Experiment	—	3	—	—	-4.4	-58.1%	
for.-cons. 3D	0.964	3	7.2	2.12	29.1	-377%	
adaptive 3D	0.743	3.12	9.7	-2.03	-11.4	8.6%	

to the case of a high stream velocity or a low turbine rotation speed, the power production is correctly estimated with both 3D models, because the local velocity is always correctly predicted. For the higher advance parameter  $\lambda = 3$  that corresponds to a high turbine rotation speed or a low stream velocity, results are less accurate. But this case is extreme with even a negative turbine power production that is small in magnitude. As a result, small discrepancies on the local velocity lead to high relative errors on the power. However the adaptive model produces less than 9 % error on the power production, and this model is suitable to estimate the power production for a wide range of advance parameters between 1 and 3.

## 4. Tidal turbine array calculations

### 4.1. The different configuration setups

The aforementioned adaptive model is used in this section to compute several configurations of turbine arrays. The 2D and 3D models are considered. The lateral spacing (distance between two consecutive turbine centers in a row) is first tested in a fence configuration, with 8 turbines side by side. A configuration of two rows of turbine with staggered positions (8 turbines in the first row, and 7 turbines in the second row) is also studied, with different lateral spacing and distances between the two rows (denoted axial spacing). The same turbine reduced-scaled model of height 17.5 cm is kept.

For all cases, a same mesh refined in the central zone around the turbines is used. It is presented in Figure 17. The constant cell height  $dz=1$  cm is used in the whole domain. Cubic cells of size  $dx=dy=dz=1$  cm are used in the central zone. The domain height is 55 cm and the turbines are lo-

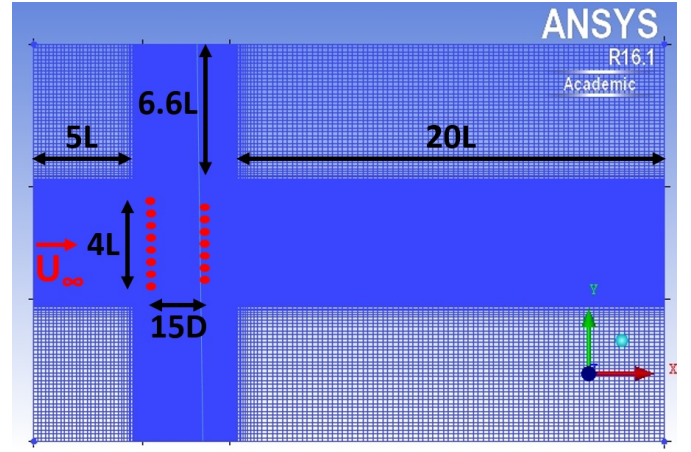


**Figure 17:** 2D view of the farm mesh and the turbine positions for the staggered configuration with 4D lateral spacing and 15D axial spacing

cated at mid-height, to remain close to real oceanic configurations where turbines are expected to occupy approximately the central third of the water column height. The central zone extends up to 18D in both y-directions, and 3D upstream and 25D downstream of the first turbine row in the x-direction. The distance  $L=7D$  is introduced as the distance between the two extreme turbine centers of a 8-turbine fence if no space is left between two adjacent turbines. An inflation of maximum growth rate 1.2 is used in the x and y directions along an upstream distance of 5L, a downstream distance of 20L, and a lateral distance of 6.6L. With this mesh the boundary conditions are far away and are not influencing the calculations anymore. The total mesh size is about 26 million cells. Symmetry conditions are used in the two lateral, the upper and the lower domain boundaries. The inlet velocity of 2.253 m/s in the x-direction is chosen. The inlet turbulence intensity is set to 2.5 %, with a value  $\omega = 1s^{-1}$  that ensures almost no turbulence decay all along the farm. The same outlet conditions as for the single machine simulations are used. A number of iterations of 20 000 is required to obtain a convergence in terms of local velocity and power production. It leads to calculation times of about 4600 core hours (on nodes Intel Sandy Bridge EP E5-2670, 8c/2.6 GHz/20M/8 GT/s with 4GB RAM/core), which is an acceptable time lower than for a single rotor URANS simulation. Moreover the domain length influence and the cell refinement in the array wake (more than 1L downstream of the array) have not been tested and it is more than likely that the cell number could be drastically reduced without significant differences in the results.

The simulations are realized with the values  $\lambda^* = 3.6$  and  $C_p^*=1.98$  in order to stay close to the optimum of power production, as explained in the former sections. All the tested farm cases are summarized in Table 3.

### 4.2. Fence configuration results

The velocity colormap and the streamlines in the horizontal plane of altitude  $z=-2$  cm are presented in Figure 18

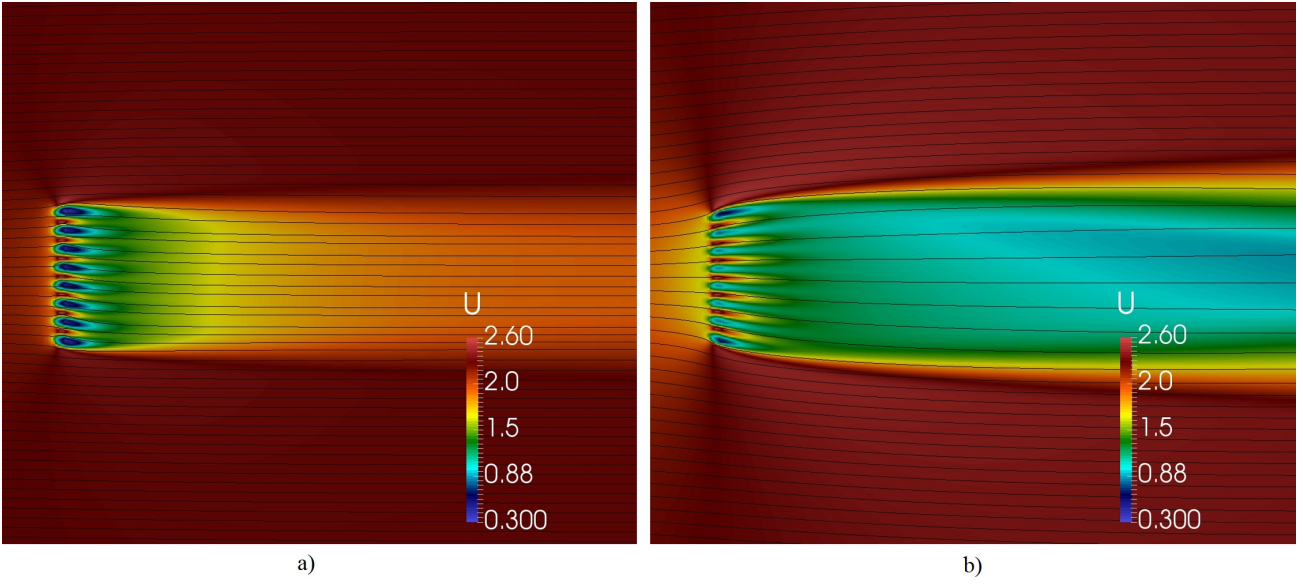


**Figure 18:** Axial velocity colormap and streamlines in the horizontal plane of altitude  $z=-2$  cm for the fence configuration with a lateral distance of  $1.2D$  between the different turbine axis, with: a) 3D model result ; b) 2D model result

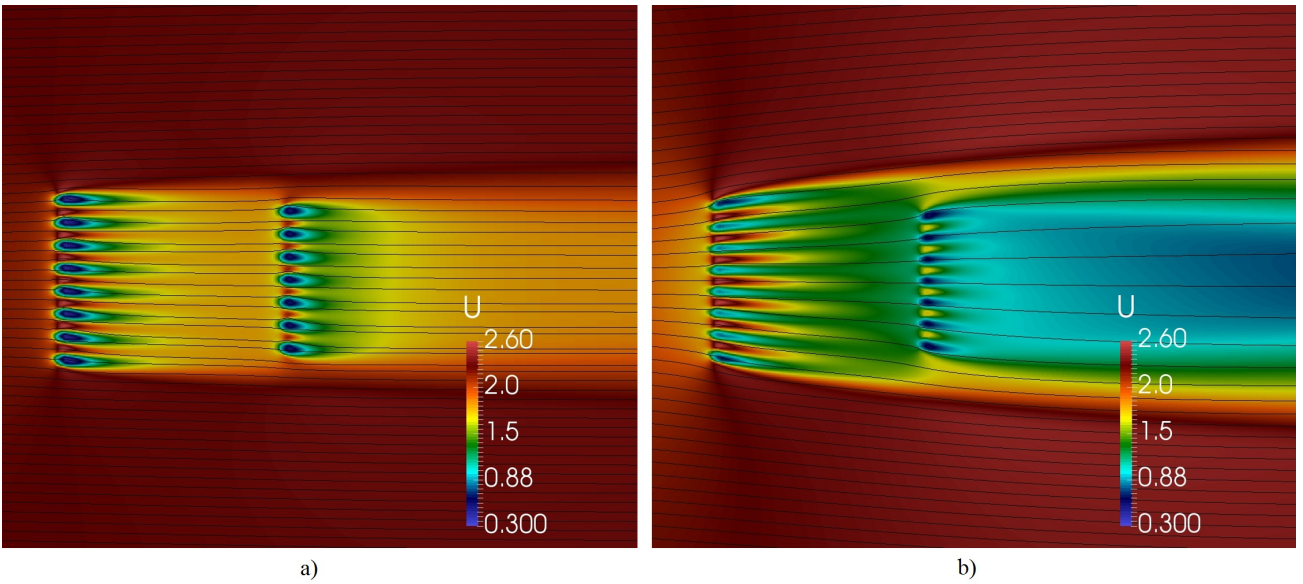


**Figure 19:** Axial velocity colormap and streamlines in the horizontal plane of altitude  $z=-2$  cm for the staggered configuration with an axial distance of  $15D$  and a lateral distance of  $1.5D$  between the different turbine axis, with: a) 3D model result ; b) 2D model result

for the fence configuration with the lateral spacing of  $1.2D$ . Both 2D model results (in the right) and 3D model results (in the left) are presented. For this spacing, the wakes of all turbines are joining to form a unique wake that continues until a distance of several  $L$  downstream of the fence. A slight global deviation of the wake towards negative  $y$ -values occurs. The velocity deficit is highly overestimated in the far-wake for the 2D model. It is in agreement with the behavior of this model that overestimates the velocity deficit for a single turbine wake (as already shown in Figure 14).

Results in term of power production are analyzed hereafter. The dimensionless farm power (DFP) is defined to

compare the total power production to the maximal one produced by the same number  $N$  of isolated turbines with the same inlet velocity, as:

$$DFP = \sum_{i=0}^N \frac{P_i}{N \times 1/2\rho SC_p^{max} U_\infty^3} \quad (12)$$

$C_p^{max} = 0.273$  is the maximal power coefficient value obtained from the URANS simulations for the less confined case in Table 1 (that is close to the non confined case). The results for the different lateral spacing are presented in Fig-

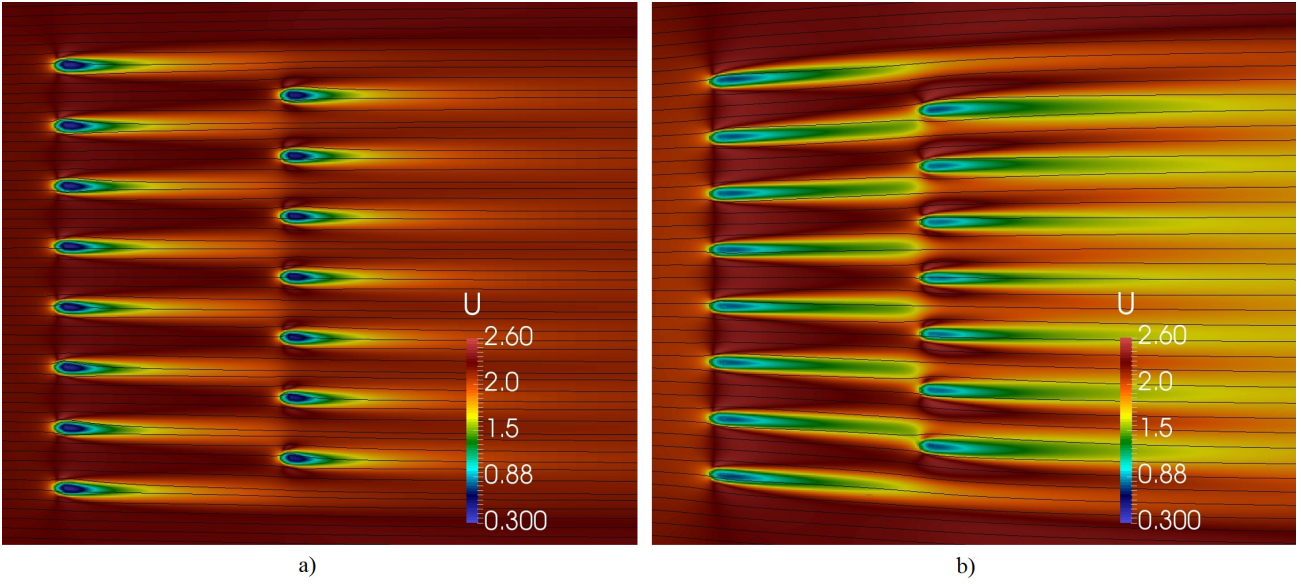


**Figure 20:** Axial velocity colormap and streamlines in the horizontal plane of altitude  $z=-2$  cm for the staggered configuration with an axial distance of  $15D$  and a lateral distance of  $4D$  between the different turbine axis, with: a) 3D model result ; b) 2D model result

**Table 3**

Inter-turbine distances for the fence farm cases and the staggered farm cases

Fence configuration				
1.2D	1.5D	2D	3D	4D
lateral spacing				
Staggered configuration				
lateral spacing		axial spacing		
1.5D	—	5D	10D	15D
4D	0D	5D	10D	15D

ure 21. The results for the same simulations using the 2D model are also shown.

In the fence, the closer the turbines are to each other, the higher the extracted power is. The same behavior is observed both in 2D and 3D. The 2D model overestimates the local blockage effect because the stream can not flow above or under the turbines. When the lateral spacing is lower than  $3D$ , a 10 to 24 % power increase is obtained compared to turbines in free stream conditions. This is coherent with results presented by McNaughton et al. (2019), that found out a power increase of 20 % for an experimental fence of two axial tidal turbines. The local blockage effect in our study is higher due to the higher number of turbines and certainly increases again the power production. Vogel and Willden (2019) found out a maximum power increase of 16 % for their 8-turbine fence simulated with a BEM method adapting to the flow conditions. The trend is respected in our simulations. However this extra-power extracted from the fluid creates a stronger velocity deficit in the wake, that might decrease the production of a potential second turbine row that

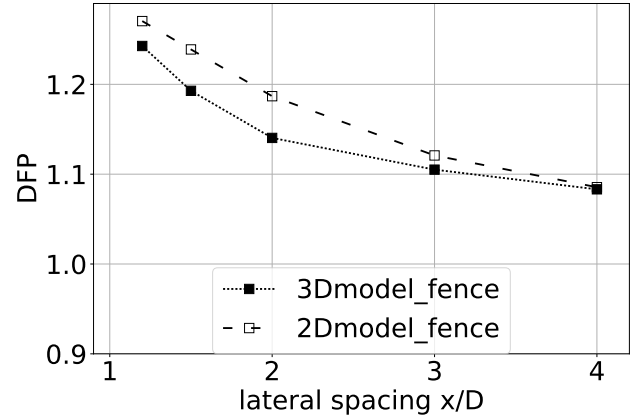


**Figure 21:** Fence dimensionless power production depending on the lateral spacing used

would be added. Therefore a two-row staggered configuration is studied in the following section.

### 4.3. Staggered configuration results

The staggered configuration wakes are presented in Figure 19 for the lateral spacing of  $1.5D$  and the axial spacing of  $15D$ , and in Figure 20 for the lateral spacing of  $4D$  and the axial spacing of  $15D$ . Both 3D model results (case a) and 2D model results (case b) are presented. In the first configuration, the velocity deficit in the wake of the first line is far higher than in the second case, where the low local blockage allows the flow in-between the turbines. The flow reaching the second row has a decreased velocity and a lower power production is expected. The global farm wake recovers also slower than for the higher lateral spacing case. In Figure 19, the velocity deficit just upstream of the second row is far

higher for the 2D model. The power production of the second row calculated with this model is expected to be small compared to the 3D model one. In Figure 20.b, the wakes of the first row turbines extend in-between the second-row turbines for the central turbines. But the first row wakes are partially impacting the 4 turbines of the second row located the most at the outsides. Therefore their power production are decreased.

The power production results of the staggered configurations are presented in Figure 22. The 3D model results are first analyzed. The solution maximizing the power production is to put all turbines on the same line (the staggered case with the axial spacing of 0D and lateral spacing of 4D is then equivalent to a 15-turbine fence with a lateral spacing of 2D). It is also noticed from Figures 21 and 22 that in this case, the DFP is 1.18, higher than the one obtained in the fence of 8 turbines with 2D lateral spacing (DFP=1.14). Adding turbines in a row increases the local blockage effect and the DFP. In the staggered cases, the lateral spacing of 1.5D hinders the flow to pass through the first row, and the flow reaching the second row witnesses a big velocity deficit. As a result, the power production of the second row is highly decreased and the dimensionless farm power is impacted, with values lower than 1. Consequences are less grave if the second row is far enough from the first one, with a dimensionless farm power higher than one for the distance 15D. For the lateral spacing of 4D, the flow is reaching the second row without any velocity deficit, and the second row witnesses even a slight local velocity increase. The farm power increase is close to 10 % for all axial spacing of the second row between 5D and 15D. The staggered configuration benefits less from the local blockage effects than the fence configuration with the same number of turbines placed close to each other. For more rows in a staggered disposition, the power harnessed is also expected to decrease if rows are too close, with better results if a bigger lateral spacing is kept between all turbines. Keeping a lateral distance sufficient enough for the stream to flow besides the first row turbines, and an axial spacing of 15D between two consecutive rows, seems enough to have a global farm wake recovery, and to enable one to put extra turbine rows without huge power decrease.

Regarding the 2D model, the same behavior is observed but there are big discrepancies on the calculated DFP values. With the lateral spacing of 1.5D, the second row power production is always highly reduced because the velocity deficit created by the first row is overestimated with the 2D model. The DFP calculated are lower than 0.8 for all those cases. The axial spacing of 15D is not enough to have a velocity deficit recover in 2D, contrary to the 3D model. For the lateral spacing of 4D, the first row wakes are expanding in-between the second row turbines when the two rows are close enough and the power production is not decreased compared to the 3D model. It starts to decrease when the axial spacing is higher than 10D. An explanation can be that some of the first row wakes are impacting the second row turbines and decreasing their power production, as already presented be-

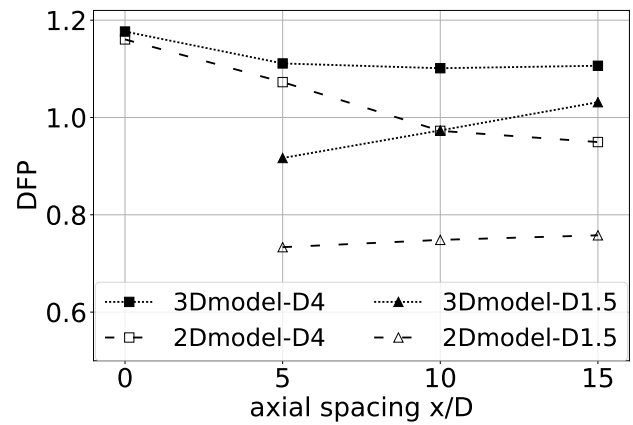


**Figure 22:** Staggered configuration dimensionless farm production depending on the axial spacing used, for the two lateral spacing tested

fore. Finally the 2D model is not accurate to compute the farm power production.

## 5. Conclusions

Different URANS blade-resolved simulations of a vertical axis Darrieus turbine have been performed to feed a steady-state 3D Actuator force model. The calculated turbine forces are time averaged over one turbine revolution to obtain a detailed spatial force distribution, instead of the uniform force distribution of standard Actuator Disk models or their equivalent for vertical axis turbines. This method replaces the classical BEM approach to obtain the force distribution.

The URANS computations have been performed for different turbine lateral confinements, in order to draw several classical power coefficient and force coefficient curves. When the coefficients are plotted as a function of the local velocity instead of the free-stream velocity, the curves become independent of the confinement. Those curves are used to construct an adaptive model independent of the turbine confinement or the local blockage effect. It gives a good estimation of the power production of a single turbine with only 3.5 % relative error at advance parameters close to the maximum efficiency point, and less than 9 % for extreme operating points. The model is also calculating correctly the far-wake flow at distances higher than 4D or 6D, but presents discrepancies for the near-wake velocity profiles.

An operating point close to the maximum efficiency point has been found for the simulated turbine. For this point, the turbine power production is calculated with an error always lower than 11.7 %, whatever the local blockage is. It is used in several farm configurations and could be a starting point for future optimization simulations, which could be performed with the model presented here that requires relatively low computational efforts.

Amongst the tested farm configurations, the fence configuration with the lowest inter-turbine spacing gives the highest farm power production. A maximum power increase of

24 % is found for the 8-turbine fence with a lateral spacing of 1.2D. Staggered farm configurations benefit less from local blockage effects even if an optimization of the lateral and axial inter-turbine spacing still has to be done. A compromise has to be found between having closely spaced first row turbines harvesting a lot of power, and still a sufficient power production in the next rows.

The same calculations have been performed using 2D models. For the single turbine simulation, the local velocity is calculated with large discrepancies, that lead to large power production discrepancies. 2D models might be sufficient to deduce general trends concerning the turbine positioning in an array, but they prove to produce large errors to calculate the array power production.

Finally the 3D model seems promising for calculating arrays of vertical axis water turbines. A comparison to measurements in the case of wake interactions between several turbines still has to be done to confirm the model. The whole methodology could also be applied to axial tidal turbines of any shape. The model validity still has to be checked for those turbines, for which the wake decay mechanisms are different.

## Acknowledgment

This work is part of the ANR 3DMMTA project funded by the french "Agence nationale de la recherche". The simulation results were obtained with the help of the GRICAD calculation mesocenter at Grenoble.

## References

- Boudreau, M., Dumas, G., 2017. Comparison of the wake recovery of the axial-flow and cross-flow turbine concepts. *Journal of Wind Engineering and Industrial Aerodynamics* 165, 137–152. <https://doi.org/10.1016/j.jweia.2017.03.010>.
- Constant, E., Favier, J., Meldi, M., Meliga, P., Serre, E., 2017. An immersed boundary method in OpenFOAM : Verification and validation. *Computers & Fluids* 157, 55–72. <https://doi.org/10.1016/j.compfluid.2017.08.001>.
- Dominguez, F., Achard, J.L., Zanette, J., Corre, C., 2016. Fast power output prediction for a single row of ducted cross-flow water turbines using a bem-rans approach. *Renewable Energy* 89, 658–670. <http://dx.doi.org/10.1016/j.renene.2015.12.042>.
- Draper, S., Nishino, T., 2014. Centred and staggered arrangements of tidal turbines. *Journal of Fluid Mechanics* 739, 72–93. <https://doi.org/10.1017/jfm.2013.593>.
- Edmunds, M., Williams, A.J., Masters, I., Croft, T.N., 2017. An enhanced disk averaged CFD model for the simulation of horizontal axis tidal turbines. *Renewable Energy* 101, 67–81. <https://doi.org/10.1016/j.renene.2016.08.007>.
- Garrett, C., Cummins, P., 2007. The efficiency of a turbine in a tidal channel. *Journal of Fluid Mechanics* 588, 243–251. <https://doi.org/10.1017/S0022112007007781>.
- Grondeau, M., Guillou, S., Mercier, P., Poizot, E., 2019. Wake of a ducted vertical axis tidal turbine in turbulent flows, lbm actuator-line approach. *Energies* 12, 22–4273. <https://doi.org/10.3390/en12224273>.
- Guillaud, N., Balarac, G., Goncalves, E., Zanette, J., 2016. Large Eddy Simulations on Vertical Axis Hydrokinetic Turbines and flow phenomena analysis. IOP Conference Series: Earth and Environmental Science 49, 102010. <https://doi.org/10.1088/1755-1315/49/10/102010>.
- Kramer, S., Piggott, M., 2016. A correction to the enhanced bottom drag parameterisation of tidal turbines. *Renewable Energy* 92, 385–396. <https://doi.org/10.1016/j.renene.2016.02.022>.
- Kramer, S., Piggott, M., Marsh, P., Ranmuthugala, D., Penesis, I., Thomas, G., 2015. Three-dimensional numerical simulations of straight-bladed vertical axis tidal turbines investigating power output, torque ripple and mounting forces. *Renewable Energy* 83, 67–77. <https://doi.org/10.1016/j.renene.2015.04.014>.
- Maître, T., Amet, E., Pellone, C., 2013. Modeling of the flow in a Darrieus water turbine : Wall grid refinement analysis and comparison with experiments. *Renewable Energy* 51, 497–512. <https://doi.org/10.1016/j.renene.2012.09.030>.
- McNaughton, J., Cao, B., Vogel, C., Willden, R.H.J., 2019. Experimental study on interactions between two closely spaced rotors, in: *Proceedings of the 7th Oxford Tidal Energy Workshop*, Oxford, UK. URL: <http://www2.eng.ox.ac.uk/tidal/ote2019-1/proceedings-ote2019>.
- Mendoza, V., Bachant, P., Ferreira, C., Goude, A., 2019. Near-wake flow simulation of a vertical axis turbine using an actuator line model. *Wind Energy* 22, 171–188. <https://doi.org/10.1002/we.2277>.
- Menter, F.R., 1994. Two-Equation Eddy-Viscosity Turbulence Models for Engineering Applications. *AIAA Journal* 32, 1598–1605.
- Menter, F.R., Kuntz, M., Langtry, R., 2003. Ten Years of Industrial Experience with the SST Turbulence Model. *Heat and Mass Transfer* 4, 625–632.
- Mycek, P., Gaurier, B., Germain, G., Pinon, G., Rivoalen, E., 2014. Experimental study of the turbulence intensity effects on marine current turbines behaviour. Part I: One single turbine. *Renewable Energy* 66, 729–746. <https://doi.org/10.1016/j.renene.2013.12.036>.
- Nguyen, V.T., Guillou, S.S., Thiébot, J., Santa Cruz, A., 2016. Modelling turbulence with an Actuator Disk representing a tidal turbine. *Renewable Energy* 97, 625–635. <https://doi.org/10.1016/j.renene.2016.06.014>.
- Nguyen, V.T., Santa Cruz, A., Guillou, S.S., Shiekh Elsouk, M.N., Thiébot, J., 2019. Three dimensional tidal turbine array simulations using OpenFOAM with dynamic mesh. *Energies* 12, 13–2468. <https://doi.org/10.3390/en12132478>.
- Nishino, T., Draper, S., 2015. Local blockage effect for wind turbines. *Journal of Physics: Conference Series* 625, 012010. <https://doi.org/10.1088/1742-6596/625/1/012010>.
- Nuernberg, M., Tao, L., 2018. Three dimensional tidal turbine array simulations using OpenFOAM with dynamic mesh. *Ocean Engineering* 147, 629–646. <https://doi.org/10.1016/j.oceaneng.2017.10.053>.
- Ordóñez-Sánchez, S., Sutherland, D., Payne, G.S., Bruce, T., Gebreslassie, M., Belmont, M.R., Moon, I., 2017. Experimental evaluation of the wake characteristics of cross flow turbine arrays. *Ocean Engineering* 141, 215–226. <https://doi.org/10.1016/j.oceaneng.2017.06.035>.
- Pope, S.B., 2000. *Turbulent Flows*. Cambridge University Press.
- Shamsoddin, S., Port'e-Agel, F., 2014. Large eddy simulation of vertical axis wind turbine wakes. *Energies* 7, 890–912. <https://doi.org/10.3390/en7020890>.
- Shives, M., Crawford, C., Grovue, S., 2017. A tuned actuator cylinder approach for predicting cross-flow turbine performance with wake interaction and channel blockage effects. *International Journal of Marine Energy* 18, 30–56. <https://doi.org/10.1016/j.ijome.2017.03.007>.
- Thiébot, J., Guillou, N., Good, A., Lewis, M., 2020. Wake field study of tidal turbines under realistic flow conditions. *Renewable Energy* 151, 1196–1208. <https://doi.org/10.1016/j.renene.2019.11.129>.
- Thiébot, J., Guillou, S., Nguyen, V.T., 2016. Modelling the effect of large arrays of tidal turbines with depth-averaged Actuator Disks. *Ocean Engineering*, 265–275.
- Vennell, R., 2013. Exceeding the Betz limit with tidal turbines. *Renewable Energy* 55, 277–285. <https://doi.org/10.1016/j.renene.2012.12.016>.
- Vogel, C., Willden, R., 2017. Multi-rotor tidal stream turbine fence performance and operation. *International Journal of Marine Energy* 19, 198–206. <https://doi.org/10.1016/j.ijome.2017.08.005>.
- Vogel, C.R., Willden, R.H.J., 2019. Improving Tidal Turbine Performance Through Multi-Rotor Fence Configurations. *Journal of Marine Science and Application* 18, 17–25. <https://doi.org/10.1007/s11804-019-00072-y>.
- Whelan, J.I., Graham, J.M.R., Peiró, J., 2009. A free-surface and blockage

correction for tidal turbines. *Journal of Fluid Mechanics* 624, 281–291.

<https://doi.org/10.1017/S0022112009005916>.

Wimshurst, A., Willden, R., 2016. Tidal power extraction on a streamwise bed slope. *Ocean Engineering* 125, 70–81.

<https://doi.org/10.1016/j.oceaneng.2016.08.007>.